Pergamon

Int. J. Heat Mass Transfer. Vol. 38, No. 14, pp. 2583–2593, 1995

0017-9310/95 $9.50+0.00

0017-9310(95)00010-0

Numerical simulation of supercritical Hadley circulation, within a porous layer, induced by inclined temperature gradients

D. M. MANOLE and J. L. LAGE†

Mechanical Engineering Department, School of Engineering and Applied Science, Southern Methodist University, Dallas, TX 75275-0337, U.S.A

(*Received* 7 *August* 1994 *and in final form* 5 *December* 1994)

Abstract—Simulations of supercritical Hadley circulation, induced by horizontal and vertical temperature gradients imposed on a fluid saturated porous medium layer, are performed numerically. The mathematical model confines the simulation to longitudinal flow in which secondary cell axes are transverse to the direction of the Hadley circulation. Numerical results agree well with critical (bifurcation) states predicted theoretically via linear stability analysis. For horizontal Rayleigh number, Ra_h, smaller than 40 and vertical Rayleigh number, Ra_v, beyond a critical value, results indicate that the flow evolves from subcritical Hadley circulation to supercritical Horton–Rodgers–Lapwood-like flow. A switch in the preferential heat transport direction, from horizontal to vertical, parallels this evolution. For Ra_h beyond 40, numerical simulations at supercritical regime reveal the appearance of a traveling wave characterized by continuous drifting of flow cells in the direction opposite to the applied horizontal temperature gradient, that is towards the cooler temperature.

1. INTRODUCTION

The present work focuses on a variation of the classical Hadley circulation phenomenon (Hart [1]) involving horizontal *and* vertical temperature gradients imposed on an infinite layer of fluid saturated porous medium confined between horizontal surfaces. This physical configuration belongs to a class of problems relevant to the study of geothermal activities, underground transport of pollutants, paper processing, crystal growth, building insulation, and gas reservoirs, just to name a few.

Studies based on linear stability analysis have thus far focused on determining the critical bifurcation states for inclined temperature gradients as in Weber [2], Nield [3–5] and for inclined temperature and concentration (double diffusion) gradients, as in Nield *et al.* [6] and Manole *et al.* [7]. The determination of stability criteria is important because the transition from one mode to another is accompanied by changes in the rate of heat and mass transports.

The characterization of the subsequent supercritical regime is fundamental for the control of thermal processes. For example, there are thermal processes that run more efficiently under subcritical state, as is the case of crystal growth in which convective (supercritical) effects are detrimental. The objective, in this case, is to maintain the process under pure conduction (subcritical) regime. Other processes run more efficiently at supercritical state, for instance thin film absorption process is enhanced by secondary (supercritical) cellular flow. A classical example of supercritical regime is the Horton–Rodgers–Lapwood (Horton and Rodgers [8] and Lapwood [9]) natural convection flow within a horizontal fluid saturated porous medium layer heated from below (or cooled from above).

A mathematical model based on Darcy's law and transient heat balance equation is presented and implemented in a numerical scheme for simulating supercritical longitudinal Hadley circulation. The circulation is induced by inclined temperature gradients within a porous medium layer. This study is aimed at investigating the fluid flow and heat transfer evolution beyond critical states (supercritical regimes).

2. MATHEMATICAL MODEL

Consider a fixed, isotropic and homogeneous porous medium bounded in the vertical direction, Fig. 1. Except for density, all physical parameters of the solid porous matrix and of the fluid are assumed constant. Regarding the density variation, the Oberbeck–Boussinesq approximation is invoked. The solid porous matrix is assumed to be in thermodynamic equilibrium with the fluid. The flow is modeled with Darcy's law [10]. Under these assumptions, the governing equations for the transport of mass, momentum and energy are :

$$\nabla \cdot \mathbf{v} = 0 \tag{1}$$

$$0 = -\nabla p - \frac{\mu}{K}\mathbf{v} - \rho(T)g\mathbf{j} \tag{2}$$

†Author to whom correspondence should be addressed.

NOMENCLATURE

c	specific heat [J kg^{-1} K^{-1}]
g	acceleration due to gravity [m s^{-2}]
H	layer height [m]
k	thermal conductivity [W m^{-1} K^{-1}]
K	permeability [m^2]
L	length [m]
l	wavelength
N	number of grid lines
Nu	Nusselt number
p	pressure [Pa]
P	non dimensional pressure, equation (7)
q	heat flux [W m^{-2}]
Ra	Darcy modified Rayleigh number, equation (7)
t	time [s]
T	temperature [K]
u, v, w	Darcy velocity components [m s^{-1}]
U, V, W	non dimensional Darcy velocity components, equation (7)
x, y, z	Cartesian coordinates [m]
X, Y, Z	non dimensional Cartesian coordinates, equation (7).

Greek symbols

α	thermal diffusivity [m^2 s^{-1}]
β	coefficient of isobaric thermal expansion [K^{-1}]
ϕ	porosity
λ	volumetric specific heat ratio, equation (7)
μ	dynamic viscosity [kg m^{-1} s^{-1}]
ν	kinematic viscosity [m^2 s^{-1}]
θ	non dimensional temperature, equation (7)
ρ	density [kg m^{-3}]
τ	non dimensional time, equation (7)
Ψ	streamfunction.

Subscripts

b	bottom
c	critical
f	fluid
h	horizontal
H	Hadley
m	fluid and solid matrix
p	preferred
r	reference
t	top
v	vertical
0	at $(x, y) = (0, 0)$.

Superscripts

n	iteration counter
$\bar{}$	(overbar) longitudinal (X) average
$'$	secondary flow.

$$(\rho c)_m \frac{\partial T}{\partial t} + (\rho c)_f (\mathbf{v}\cdot\nabla T) = k_m \nabla^2 T \qquad (3)$$

where $\mathbf{v} = u\mathbf{i} + v\mathbf{j} + w\mathbf{k}$ is the Darcy velocity and $(\mathbf{i}, \mathbf{j}, \mathbf{k})$ are unit vectors parallel to (x, y, z) Cartesian axis, respectively. The boundary conditions for velocity and temperature are :

$$v = 0 \quad \text{at} \quad y = 0 \quad \text{and} \quad H \qquad (4)$$

$$T = T_0 + \frac{\Delta T_h}{L} x \quad \text{at} \quad y = 0 \qquad (5)$$

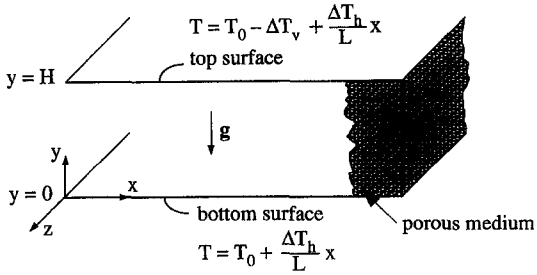

Fig. 1. Physical model and applied temperature gradients.

$$T = T_0 - \Delta T_v + \frac{\Delta T_h}{L} x \quad \text{at} \quad y = H. \qquad (6)$$

With physical parameters defined in the nomenclature, the system of equations (1)–(3) and boundary conditions listed in equations (4)–(6) are non dimensionalized using :

$$(X, Y, Z) = \frac{(x, y, z)}{H}, \quad \mathbf{V} = \frac{\mathbf{v}}{\alpha_m / H}, \quad P = (p + \rho g y)\frac{K}{\rho \nu \alpha_m}$$

$$\lambda = \frac{(\rho c)_m}{(\rho c)_f}, \quad \tau = \frac{\alpha_m t}{\lambda H^2}, \quad \theta = \frac{T - T_r}{\Delta T_v}$$

$$Ra_v = \frac{g\beta K H \Delta T_v}{\nu \alpha_m}, \quad Ra_h = \frac{g\beta K H^2 \Delta T_h}{\nu \alpha_m L}, \quad T_r = \frac{\Delta T_v}{2}$$

$$\rho(T) = \rho[1 - \beta(T - T_r)], \quad \alpha_m = \frac{k_m}{(\rho c)_f}. \qquad (7)$$

The non-dimensional form of the system of equations (1)–(3) is then

$$\nabla \cdot \mathbf{V} = 0 \qquad (8)$$

$$0 = -\nabla P - \mathbf{V} + Ra_v \theta \mathbf{j} \qquad (9)$$

$$\frac{\partial\theta}{\partial\tau}+\mathbf{V}\cdot\nabla\theta=\nabla^2\theta \tag{10}$$

where $\mathbf{V}=U\mathbf{i}+V\mathbf{j}+W\mathbf{k}$. The boundary conditions, in non-dimensional form, are

$$V=0 \quad \text{at} \quad Y=0 \quad \text{and} \quad 1 \tag{11}$$

$$\theta=\theta_0+\frac{Ra_h}{Ra_v}X \quad \text{at} \quad Y=0 \tag{12}$$

$$\theta=\theta_0-1+\frac{Ra_h}{Ra_v}X \quad \text{at} \quad Y=1. \tag{13}$$

A steady state solution of the system of equations (8)–(10), known as Hadley circulation [1], is

$$U_H=-Ra_h(Y-0.5) \tag{14}$$

$$V_H=W_H=0 \tag{15}$$

$$\theta_H=\frac{Ra_h}{Ra_v}X+\theta_0-Y+\frac{Ra_h^2}{Ra_v}\frac{1}{24}[(Y-0.5)-4(Y-0.5)^3]. \tag{16}$$

It is worth noting that the stability analysis presented by Weber [2], and refined by Nield [4], indicated that the solution presented by equations (14)–(16) bifurcates whenever Ra_v increases beyond a critical value, Ra_{v_c}, for fixed Ra_h. Noting that the basic flow (Hadley circulation) is Z-independent, equations (8)–(10) can be restricted to the Z plane. This implies that the secondary flow is restricted to horizontal rolls with axis perpendicular to the imposed horizontal temperature gradient (transverse mode of disturbances), a situation expected to occur when Z to X length ratio of the porous layer is relatively small.

For transverse secondary flow, the two dimensional version of equations (8)–(10) is solved numerically with boundary conditions listed in equations (11)–(13). The present model is valid also for salinity driven convection if one replaces T by concentration C, thermal diffusivity by mass diffusivity, and isobaric coefficient of thermal expansion by solutal expansion coefficient. Nield [4] indicated that for Ra_h smaller than 40 the flow bifurcation is to a stationary mode for increasing Ra_v. For larger Ra_h, the corresponding expected bifurcation is to a time-dependent oscillatory mode.

3. NUMERICAL METHOD

Convection generated by inclined temperature gradients within an infinite horizontal layer presents the following characteristics : (1) the basic steady state flow (Hadley circulation) is invariant with the longitudinal coordinate, X and (2) the secondary convective flow that is expected to develop at supercritical state ($Ra_v > Ra_{v_c}$) must be periodic in the longitudinal direction, with period l. With these in mind, the non dimensional length of the numerical domain, L/H, is considered to be a multiple of l, the wavelength of the secondary flow. Consequently, the velocity boundary conditions at the vertical surfaces of the numerical domain have to satisfy :

$$U(0, Y)=U(L/H, Y), \quad V(0, Y)=V(L/H, Y). \tag{17}$$

Over a distance L/H, the horizontal temperature gradient induces an increase equal to $\Delta\theta_h$ on the temperature of the basic flow. Since the secondary convective flow is periodic within L/H, the appropriate temperature vertical boundary condition is

$$\theta(0, Y)=\theta(L/H, Y)-\Delta\theta_h. \tag{18}$$

The control volume method (Patankar and Spalding [11]) is used for solving the two dimensional version of equations (8)–(10) with SIMPLER algorithm and Power Law scheme (Patankar [12]). Staggered grids (Harlow and Welch [13]) are used, where pressures (and temperatures) are evaluated at locations different from those where the velocities are evaluated. Integration in time of the energy equation is performed fully implicitly. Although the aim of the present work is not to simulate the bifurcation phenomena, the programming was done carefully enough so that numerical results could be compared with theoretical predictions of critical states, helping validate the code. A very interesting study that demonstrates the use of the control volume method for simulating bifurcation to time periodic natural convection flow was presented by Janssen *et al.* [14].

Although being of Dirichlet type, the velocity and temperature vertical boundary conditions, equations (17) and (18), do not set a specific value of the variable at the boundary, but rather, they simply specify a relationship between the values at the two vertical boundaries of the numerical domain. Combined with the possibility of tilted secondary flow cells interface, as indicated next, the handling of the boundaries of the numerical domain required extra care.

Mehta [15], in a similar inclined gradient problem (double-diffusive) showed that the critical flow cells interface might be tilted under certain circumstances. Further evidence that cells interface might be tilted was given by Sarkar and Phillips [16] in their study of thermohaline instabilities in a saturated infinite porous medium. For large horizontal temperature gradients, Sarkar and Phillips [17] investigated also the roll development within a saturated and thick layer of porous medium. Tilted cell interfaces were revealed at critical stability state.

It is evident that in general the interface between two adjacent secondary flow cells might not be vertical. Therefore, imposing impermeable boundary conditions for the secondary flow at the vertical surfaces of the numerical domain is too restrictive.

Figure 2 shows a special choice of discretization in the X direction that allows for the implementation of the boundary conditions, the appearance of tilted cells interface, and yet efficient computation. The grid has been *rolled* in the figure for an easier identification of the vertical grid lines to which the periodic properties

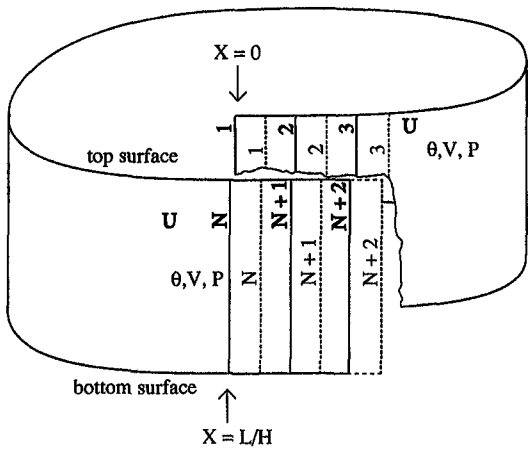

Fig. 2. Vertical grid lines distribution for periodic vertical boundary conditions.

of the convective flow are applied. Consider the original numerical domain, limited by $X = 0$ and $X = L/H$, discretized in the horizontal direction with N lines where velocity U is computed. The actual numerical domain is extended beyond these limits by adding two additional lines, $(N+1)$ and $(N+2)$. In this way, with boundary conditions (17), the value of the velocity at line 1 is updated with the computed value at interior line N. By the same token, the value of the velocity at line $(N+2)$ is updated with the value computed at interior line 3.

Extending the domain by two lines induces periodicity of first derivatives also, enhancing the numerical convergence of the code specially during the initial phase of the iteration process. Furthermore, it allows for an indirect verification that the obtained numerical solution is indeed periodic. This is accomplished by comparing the velocity values computed at lines 2 and $(N+1)$. These are the first interior lines of the numerical domain, and their values must be the same, for each Y, if the solution is perfectly periodic. (Recall that the boundary conditions are applied at lines 1 and $N+2$ only.)

Vertical boundary conditions for temperature are handled in a similar fashion, where the dashed lines shown in Fig. 2 locate the temperature nodes. The temperatures at the interior lines, from 2 to $N+1$, are computed. Applying boundary condition (18), the temperatures at line 1 become equal to the temperatures at line N minus the temperature difference $\Delta\theta_h$, and so on.

The convergence criterion used in here is based on a max-norm of the top and bottom vertical Nusselt number (defined in the following section, equation (22)),

$$\mathrm{MAX}\left[\left|\frac{\overline{Nu}^{n}_{v_{t,b}} - \overline{Nu}^{n+1}_{v_{t,b}}}{\overline{Nu}^{n}_{v_{t,b}}}\right|\right] \leqslant 10^{-6} \qquad (19)$$

where n and $n+1$ are two consecutive iterations.

The grid is uniformly distributed, with same grid step in both directions. Grid accuracy tests are performed comparing the theoretical solution for the base flow (Hadley circulation) with numerical results obtained for subcritical states. For instance, using 1/20 grid step, for $Ra_h = 10$, $Ra_v = 40$, the maximum difference in velocity and temperature are respectively 0.011% and 0.046%. Results for supercritical regimes are estimated using 1/20 grid step and subsequently refined by reducing the grid step in 30% until consecutive results change by less than 4%.

4. RESULTS AND DISCUSSION

The choice of Rayleigh number values used in the numerical simulations is based essentially on the bifurcation criteria to supercritical regime as established by Nield [4]. The vertical Rayleigh number, defined as in equation (7), is the same as the vertical Rayleigh numbers used by Weber [2] and Nield [4]. The horizontal Rayleigh number is also the same, provided β^* used by Nield [4] be replaced with $(\Delta T_h/L)$. Note also that for small Darcy number and large Prandtl number, the Darcy model is expected to be reasonably accurate within the Ra_v range investigated here, as far as inertial effects are concerned (Lage [18]).

Horizontal and vertical Nusselt numbers, representing the energy transported by convection and conduction in each direction, are defined respectively as

$$Nu_h(X) = \frac{q_h}{k_m \dfrac{\Delta T_h}{L}} = \frac{\dfrac{1}{H}\displaystyle\int_0^H \left[\rho u c_p (T - T_r) - k_m \frac{\partial T}{\partial x}\right] dy}{k_m \dfrac{\Delta T_h}{L}} = \frac{Ra_v}{Ra_h}\int_0^1 \left(U\theta - \frac{\partial \theta}{\partial X}\right) dY \qquad (20)$$

$$Nu_v(X, Y) = \frac{q_v}{k_m \dfrac{\Delta T_v}{H}} = \frac{\left[\rho v c_p (T - T_r) - k_m \dfrac{\partial T}{\partial y}\right]}{k_m \dfrac{\Delta T_v}{H}} = \left(V\theta - \frac{\partial \theta}{\partial Y}\right). \qquad (21)$$

Corresponding non-dimensional wavelength-averaged top and bottom vertical heat fluxes, $\overline{Nu}_{v_t}$ and $\overline{Nu}_{v_b}$, and horizontal heat flux, $\overline{Nu}_h$, are calculated as follows:

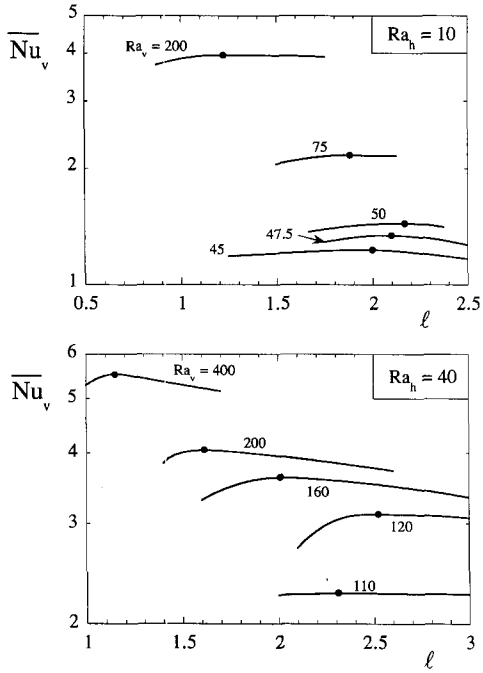

Fig. 3. Wavelength averaged vertical Nusselt number : top, $Ra_h = 10$; bottom, $Ra_h = 40$.

$$\overline{Nu}_{v_t} = \frac{1}{l}\int_0^l Nu_v|_{Y=0}\,dX$$

$$\overline{Nu}_{v_t} = \frac{1}{l}\int_0^l Nu_v|_{Y=1}\,dX$$

$$\overline{Nu}_h = \frac{1}{l}\int_0^l Nu_h\,dX. \qquad (22)$$

For each group (Ra_v, Ra_h) the length of the numerical domain, L/H, is varied since no information is available on the wavelength of the supercritical secondary flow. For each length, a wavelength, l, is determined by dividing (L/H) by the number of patterns present in the flow. Obviously, whenever the secondary flow effects are negligible the length of the numerical domain becomes irrelevant since the base flow (Hadley circulation) is X independent.

Figure 3 presents the vertical Nusselt number variation with wavelength for Ra_h equal to 10 (top) and 40 (bottom), and several Ra_v. All simulations have converged to a steady-state solution with $\overline{Nu}_{v_t} = \overline{Nu}_{v_b} = \overline{Nu}_v$. Dots indicate the values of l that maximize the vertical heat transfer. Invoking the maximum heat transport hypothesis introduced by Malkus [19], these values are taken as the preferential wavelengths, l_p, of the system. It is important to stress that although it is known that for Horton–Rodgers–Lapwood convection the Malkus hypothesis underpredicts the preferred wavelength of the flow (Combarnous and Bories [20]), the heat transfer predictions agree well with experiments as indicated by Busse and Joseph [21] and Gupta and Joseph [22].

Also, the heat transfer results presented in Fig. 3 are very weakly dependent on wavenumber, therefore the discussion on the validity of Malkus hypothesis is not important since the focus of the present work is on heat transfer phenomena. In fact, for low Ra_v the Nusselt number value obtained is reasonably accurate if the wavelength predicted by the linear stability analysis study of Nield [4] is taken as preferred wavelength for supercritical regimes.

Table 1 offers the first indication that the flow regime, at low horizontal Rayleigh number, evolves from subcritical Hadley flow to Horton–Rodgers–Lapwood-like flow. In it, Nusselt and wavelength values obtained for the case $Ra_h = 10$, are compared with the Nusselt values of Hadley flow, Nu_{v_H}, and with the results obtained by Lage [18] and Gupta and Joseph [22] for Horton–Rodgers–Lapwood flow. The Hadley flow based Nusselt number, Nu_{v_H}, is obtained by using equations (14)–(16) into the vertical Nusselt definition, equation (22). As Ra_v increases, the averaged vertical Nusselt number, $\overline{Nu}_v$, seems to depart from the vertical Nusselt number value of Hadley circulation, Nu_{v_H}, tending to values similar to the Nusselt number values of the Horton–Rodgers–Lapwood flow.

Attention is now turned to the deviation from the basic flow (Hadley circulation) as Ra_v increases. Figure 4 (left) shows the flow evolution, streamlines of the main flow and of the secondary flow, as Ra_v

Table 1. Comparison of preferred wavelength, l_p, and vertical Nusselt number, $\overline{Nu}_v$, with Hadley flow Nusselt number, Nu_{v_H}, Nusselt number, Nu_v^L, obtained by Lage [18], and Nusselt number, Nu_v^{GJ}, and wavelength, l_p^{GJ}, obtained by Gupta and Joseph [22]

	Numerical results			Lage [18]	Gupta and Joseph [22]§		
Ra_v	l_p	$\overline{Nu}_v$	Nu_{v_H}	Nu_v^L‡	Ra_v^{GJ}	l_p^{GJ}	Nu_v^{GJ}
40	—	1.21	1.21	—	39.48	2.00	1.00
45	2.01	1.23	1.19	—	—	—	—
47.5	2.10	1.34	1.18	—	—	—	—
50	2.17	1.45	1.16	1.44	49.2	1.98	1.43
75	1.87	2.16	1.11	—	76.5	1.81	2.27
200†	1.27	3.95	1.04	3.76	207	1.17	5.07

†Experimental results for $Ra_v = 200$: $l_p \sim 1.82$, $Nu_v = 2.8$–5.6 (Combarnous and Bories [20]).
‡Numerical results for Horton–Rodgers–Lapwood convection with wavelength equal to 2.
§Predictions in agreement with experiments (see Nield and Bejan, [23], p. 163).

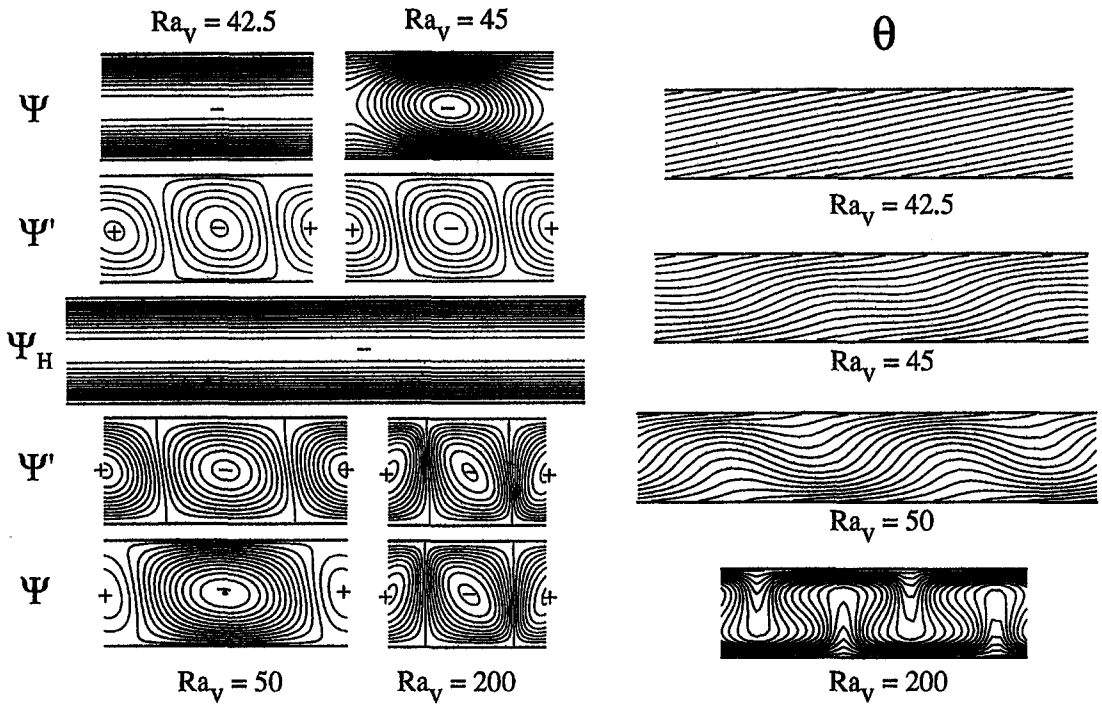

Fig. 4. Streamlines (left) and isotherms (right) for $Ra_h = 10$. Ψ, main flow ; Ψ', secondary flow ; Ψ_b, Hadley flow ; (+), counter clockwise rotation ; (−), clockwise rotation (Ψ increment : 10^{-3}, 0.1, 0.2, 1, for $Ra_v = 42.5$, 45, 50 and 200, respectively).

increases using the preferred wavelength value indicated in Table 1. The streamlines of the Hadley flow, Ψ_H, are also presented for reference. The secondary streamline distribution, Ψ', is obtained by subtracting the Hadley streamfunction, Ψ_H, from the flow streamfunction, Ψ,

$$\Psi' = \Psi - \Psi_H \tag{23}$$

where streamfunctions are defined by

$$\frac{\partial(\Psi, \Psi_H, \Psi')}{\partial Y} = (U, U_H, U')$$

$$\frac{\partial(\Psi, \Psi_H, \Psi')}{\partial X} = -(V, V_H, V'). \tag{24}$$

The Ψ-streamlines for $Ra_v = 42.5$ are very similar to the Ψ_H-streamlines of a Hadley circulation, indicating the weakness of the secondary flow. As Ra_v increases ($Ra_v = 45$), the Ψ-streamlines show the growth of a cell rotating in the same sense as the Hadley circulation. Other cells, rotating in the opposite sense, develop around the initial cell at about $Ra_v = 50$. Their intensity keeps growing with Ra_v. At $Ra_v = 200$, all cells assume almost the same size, with consecutive cells being counter rotating, similar to the Horton–Rodgers–Lapwood flow. Notice that the Ψ'-streamlines are of similar shape with counter rotating consecutive cells throughout the Ra_v evolution. Evidently, the strength of this secondary flow is enhanced as Ra_v increases.

The evolution of the flow can be explained by focusing on the superposition of Hadley and secondary flows. At low Ra_v, the secondary cell that rotates counter clockwise (−) has its horizontal velocity component in the same sense as the Hadley velocity, so its effect is amplified by the Hadley flow. The secondary flow cell that rotates clockwise (+) is subdued by the Hadley circulation since its horizontal velocity is in opposite sense. The result is the elongated horizontal

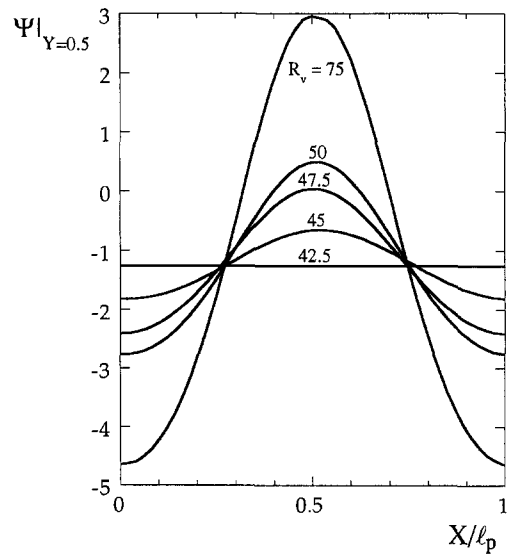

Fig. 5. Streamfunction at mid height ($Y = 0.5$) vs normalized X for $Ra_h = 10$.

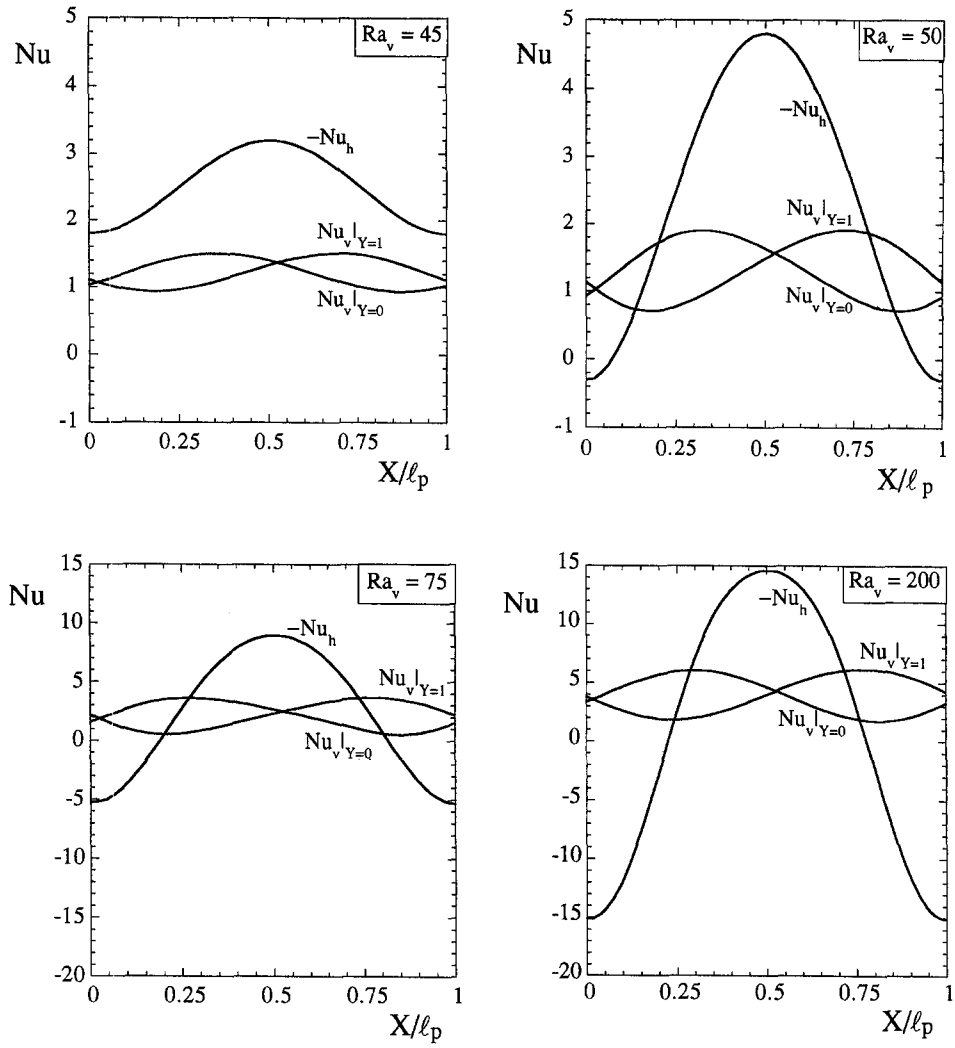

Fig. 6. Local top ($Nu_v|_{Y=1}$) and bottom ($Nu_v|_{Y=0}$) vertical and horizontal (Nu_h) Nusselt numbers for $Ra_h = 10$.

counter clockwise cell shown at $Ra_v = 45$, for instance. As Ra_v increases further and the secondary flow strengthens, the clockwise secondary cell eventually overcomes the opposite Hadley circulation, that is when the clockwise rotating cells appear in the main flow ($Ra_v = 50$). Furthermore, the enhancing effect of the Hadley flow on the counter clockwise secondary cells is proportionally reduced. At $Ra_v = 200$, the strength of the Hadley flow becomes negligible when compared with the secondary flow, explaining why a Horton–Rodgers–Lapwood-like flow sets in.

Also evident is that the interface between consecutive cells is increasingly tilted as Ra_v is reduced. The angle, in degrees, between a vertical line and the interface line is approximately equal to 0.0, 2.1, 2.6, 8.4 and 11.7 for Ra_v equal to 200, 75, 50, 45 and 42.5, respectively.

The corresponding isotherms, plotted in Fig. 4 (right), also suggest the transition from Hadley flow to Horton–Rodgers–Lapwood-like flow as Ra_v increases. The isotherms become more concentrated near the horizontal surfaces (consequence of the better mixing) indicating thinner thermal boundary layers and, consequently, increased vertical heat transfer coefficient. The isotherms pattern indicates also periodicity in the horizontal and vertical heat transfer coefficients.

Figure 5 offers evidence that the bifurcation state, simulated numerically, is very close to the theoretical value. In it, the streamfunction at mid layer ($Y = 0.5$) is plotted against the horizontal direction normalized with the respective preferred wavelength, X/l_p, for several Ra_v. For Hadley circulation, the streamfunction curve is expected to be horizontal (since the flow is X-independent) and equal to -1.25. The value for $Ra_v = 42.5$ varies from -1.11 to -1.39, averaging -1.25. Results for $Ra_v = 42$ show, within the accuracy of the present numerical simulation, a streamfunction value uniformly equal to -1.25 with no secondary flow pattern being identified.

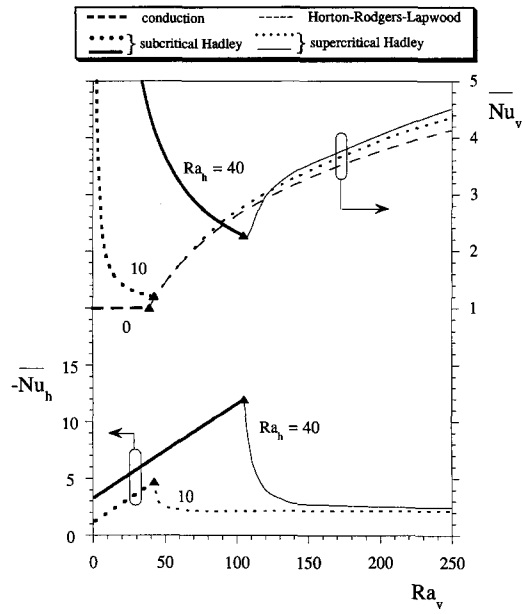

Fig. 7. Wavelength averaged vertical and horizontal Nusselt numbers.

From the linear stability analysis result of Nield [4], specifically his equation (31) for $Ra_h = 10$, the critical wavelength value and critical vertical Rayleigh number for onset of transverse instability are approximately 2.03 and 43.9, respectively. Taking into account the differences between the two methods, the agreement is remarkable.

Figure 6 shows, for $Ra_v = 45$, 50, 75 and 200, the longitudinal variation of horizontal and top and bottom vertical Nusselt numbers. The negative of the horizontal Nusselt number values are plotted to improve readability of the graphs. The horizontal Nusselt number for Hadley circulation is constant in X and equal to 2.6, 3.0, 5.1 and 15.5, for $Ra_v = 45$, 50, 75 and 200, respectively. The wavelength-averaged horizontal Nusselt number decreases with Ra_v, reflecting the influence of the secondary flow (the cellular form of the secondary flow is detrimental to the convection of heat in the horizontal direction). At $Ra_v = 200$ the wavelength-averaged horizontal Nusselt number is close to zero as expected.

Vertical Nusselt numbers at $Y = 1$ and at $Y = 0$ show central symmetry as expected. The profiles follow the convective effect of circulating cells, with maximum Nu_v near the region of incoming vertical stream.

Figure 7 presents the wavelength averaged vertical (top) and horizontal (bottom) Nusselt numbers variation with Ra_h and Ra_v. Notice that the negative of the horizontal Nusselt number is plotted for convenience. The thick lines (to the left) denote the subcritical regime, with dashed line referring to conduction regime ($Ra_h = 0$) and dotted and continuous lines referring to Hadley flow ($Ra_h > 0$). Thin lines show the variation of the Nusselt numbers once the supercritical regime is established. The $\overline{Nu}_v$ values for Horton–Rodgers–Lapwood regime ($Ra_h = 0$) are those reported by Lage [18]. The black triangles locate the numerically estimated critical states. The Nusselt number for Hadley flow regime can be obtained numerically. It can be obtained also theoretically by using the temperature distribution, equation (16), and the Nusselt definitions, equations (20)–(22). The theoretical approach indicates that the averaged vertical Nusselt number for Hadley regime is function of Ra_h^2/Ra_v, that is why its value tends to infinity as Ra_v tends to zero with Ra_h constant. This result has to be taken cautiously : it is not the vertical dimensional heat flux that is tending to infinity as Ra_v decreases but rather the vertical temperature difference used to non dimensionalize the heat flux is going to zero (see equation (21)).

Figure 7 is critical from an engineering standpoint. It conjoins the heat transfer information of two distinct and predominating flow regimes : subcritical (basic) Hadley flow and supercritical Hadley flow. It is clear that the ability of the basic Hadley flow to transfer heat in the vertical direction becomes increasingly hindered when the vertical Rayleigh number is increased. At the critical state, the secondary flow sets in providing a more effective path for heat to be transferred through the horizontal surfaces of the porous layer. Further increase in Ra_v enhances heat transfer in the vertical direction. It also reduces heat transfer in the horizontal direction. The results show also that the Hadley flow is slightly beneficial to the

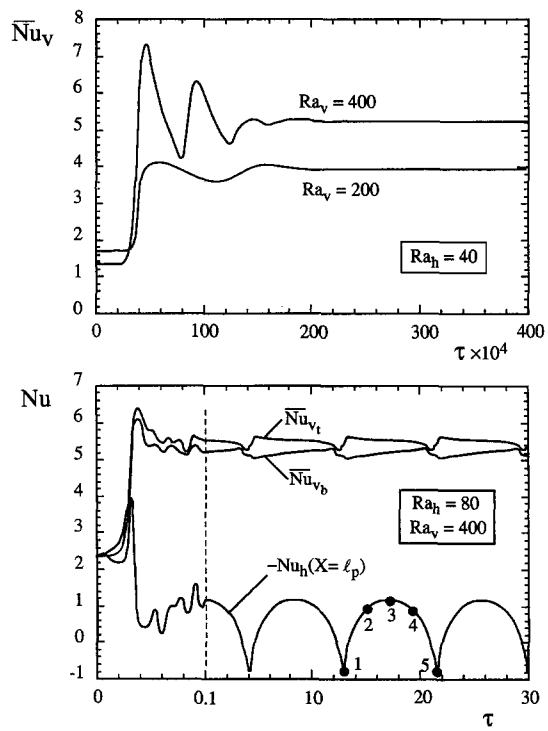

Fig. 8. Time evolution of Nusselt number : top, $Ra_h = 40$; bottom, $Ra_h = 80$.

vertical heat transport at supercritical Ra_v when compared with the heat transfer provided by Horton–Rodgers–Lapwood flow.

5. TRANSITION TO TRAVELING WAVE REGIME

Figure 8 presents the time evolution of the top and bottom vertical wavelength averaged Nusselt numbers. The top graph shows results for $Ra_h = 40$ and $Ra_v = 200$ and 400. Both vertical Nusselt values, top and bottom, coincide for each Ra_v. Also evident in both curves is the initial oscillatory behavior. Oscillation amplitude and frequency are intensified as Ra_v increases. Numerical results indicated a critical state at $Ra_v \approx 108$. This Nusselt behavior agrees well with Nield's [4] prediction of transition from transverse stationary mode to transverse oscillatory mode at $Ra_h = 40$, with Ra_{v_c} equal to approximately 118.

In the bottom graph, for $Ra_h = 80$ and $Ra_v = 400$, the oscillations persist throughout the simulation, indicating an oscillatory regime. In this case top and bottom Nusselt numbers are distinct in time during most of the cycling. Also cyclic is the variations of the horizontal Nusselt number computed at $X = l_p$. All curves cycle at the same frequency of about 1.17×10^{-1}. Coincidentally, whenever the vertical Nusselt numbers diverge, the horizontal one increases, allowing for the excess heat to flow in the horizontal direction. During one cycle, the time averaged vertical, top and bottom, and horizontal Nusselt values are 5.51, 5.33 and 0.72. Finally, observe that the horizontal Nusselt number oscillates between a negative and a positive value. In a cellular flow, this can occur if a fixed (in space) cell tilts periodically (in time) around a vertical axis, or if moving cells, with opposite tiltness, cross periodically the location $X = l_p$. It is shown next that the latter describes the phenomenon correctly.

Figure 9 presents the time evolution, during one cycle, of streamlines (left) and isotherms (right) for

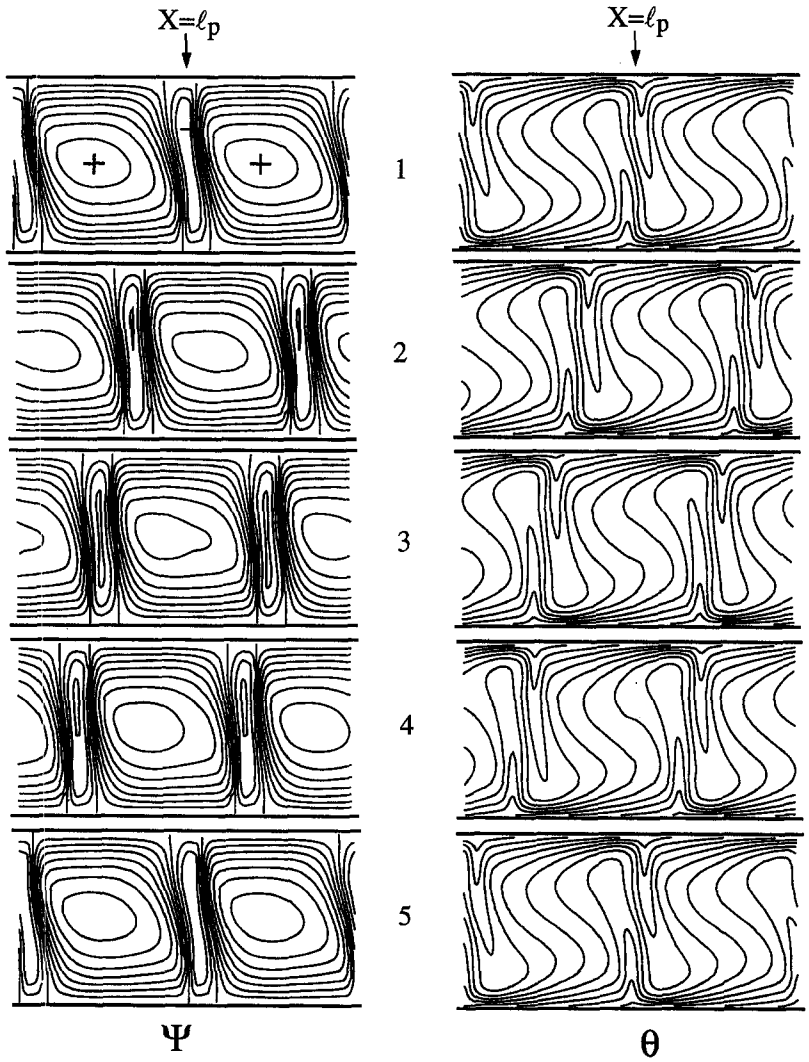

Fig. 9. Streamlines and isotherms temporal evolution during one cycle : $Ra_h = 80$; $Ra_v = 400$; (+), counter clockwise rotation ; (−), clockwise rotation.

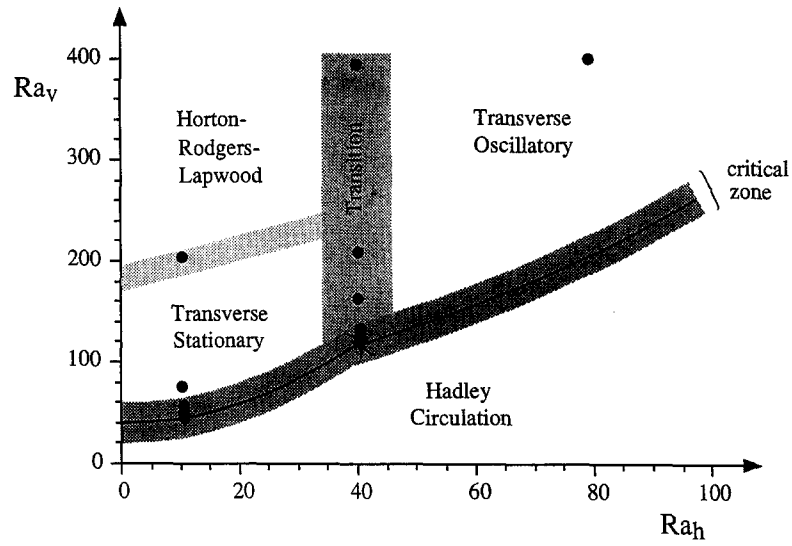

Fig. 10. Qualitative mapping of preferred flow configuration ; ●, simulations performed in the present study.

$Ra_h = 80$ and $Ra_v = 400$. Each sequence of five frames (equally spaced in time) follows the numbered dots included for reference in the bottom graph of Fig. 8. The two cells, with approximately 5 : 1 width ratio, constitute a flow pattern. The vertical axis of the cells are tilted, and the tiltness varies slightly in time as the cells move (drift) from right to left. The larger cell rotates counter clockwise, being horizontally stretched by the basic Hadley circulation. The opposite is the case of the smaller cell that tends to break vertically into two cells (see streamlines at the center of smaller cell during frame sequence 2–3–4).

Not so evident from these pictures is the change in the rate of drifting. Looking closely at one interface streamline (e.g. one vertical line separating the small cell from the big cell), and following its motion, it can be seen that the horizontal distance traveled by this line from frame 1 to 2 is different from the distance traveled by it from frame 2 to 3, for instance. A numerical visualization technique developed during this project allows a more sensible observation that the drifting rate varies in time. Isotherms evolution shows that the small cell deforms the temperature field more vigorously than the larg cell.

Again the main features of the oscillatory flow agree qualitatively with those anticipated by the stability analysis of Nield [4]. The phenomenon presented in Fig. 9 is that of an irregular (with respect to speed) traveling wave. The non dimensional averaged wave speed is approximately equal to $2.34 \times 10^{-3}/\phi$.

Finally, the numerical investigation performed here is best summarized with the qualitative mapping of several flow phenomena, Fig. 10. The inclusion of the critical state curves (solid lines after Nield [4]) is helpful in delineating the fundamental transitions from Hadley circulation to transverse stationary flow ($Ra_h < 39.5$) and to transverse oscillatory flow ($Ra_h > 39.5$). Results presented in this study are for configurations indicated with dots in Fig. 10.

6. CONCLUSIONS

Simulations of supercritical Hadley circulation induced by inclined temperature gradients, within a fluid saturated porous layer, are performed numerically. The parametric range of the present investigation is guided by the linear stability analysis results published in the literature. Numerical results presented in here are checked against stability results showing remarkably good agreement.

For horizontal Rayleigh number smaller than approximately 40, the transition from Hadley circulation occurs with the appearance of transverse flow cells as the vertical Rayleigh number is increased. It is verified that for Ra_v beyond approximately 200 the flow becomes cellular dominated, similar to Horton–Rodgers–Lapwood flow. The oscillations occur at modest values of Rayleigh numbers, where the mechanism is different from that producing oscillations at high values of Rayleigh numbers. As Nield [4] pointed out, the oscillations are essentially a thermal phenomenon, and involve a switching between two steady-state modes.

At Ra_h around 40 and Ra_v above the critical value (supercritical flow), a transition zone is detected in which the heat transfer evolves following an oscillatory behavior that decays in time. The amplitude and frequency of these oscillations increase as Ra_v increases.

At Ra_h larger than 40, the transition is from Hadley circulation to oscillatory flow, as Ra_v increases. The oscillatory flow, in the form of a traveling wave, is characterized by the following main aspects: (1) flow pattern of two cells with width ratio 5 : 1; (2) flow

drifting in the direction opposite to the imposed horizontal temperature gradient, that is towards the cooler temperature; (3) oscillatory tilting of vertical cell axis and (4) non uniform drifting speed. Some of these characteristics agree with those anticipated by Nield [4].

Acknowledgements—Dr Manole acknowledges the Ph.D. scholarship provided by the Center for Porous Material Applications of the Mechanical Engineering Department. Professor Lage is grateful for the support provided by the "J. L. Embrey Professorship" in Mechanical Engineering. Review of an earlier draft by Professor Nield is appreciated. We are thankful for the enlightening comments and suggestions by the reviewers.

REFERENCES

1. J. E. Hart, Stability of Thin Non-rotating Hadley Circulations, *J. Atmos. Sci.* **29,** 687–697 (1972).
2. J. E. Weber, Convection in a porous medium with horizontal and vertical temperature gradients, *Int. J. Heat Mass Transfer* **17,** 241–248 (1974).
3. D. A. Nield, Convection in a porous medium with inclined temperature gradient and horizontal mass flow, *Heat Transfer* **5,** 153–158 (1990).
4. D. A. Nield, Convection in a porous medium with inclined temperature gradient, *Int. J. Heat Mass Transfer* **34,** 87–92 (1991).
5. D. A. Nield, Convection in a porous medium with inclined temperature gradient : additional results, *Int. J. Heat Mass Transfer* **37,** 3021–3025 (1994).
6. D. A. Nield, D. M. Manole and J. L. Lage, Convection induced by inclined thermal and solutal gradients in a shallow horizontal layer of a porous medium, *J. Fluid Mech.* **257,** 559–574 (1993).
7. D. M. Manole, J. L. Lage and D. A. Nield, Convection induced by inclined thermal and solutal gradients, with horizontal mass flow, in a shallow horizontal layer of a porous medium, *Int. J. Heat Mass Transfer* **37,** 2047–2057 (1994).
8. C. W. Horton and F. T. Rodgers, Convection currents in a porous medium, *J. Appl. Phys.* **16,** 367–370 (1945).
9. E. R. Lapwood, Convection of a fluid in a porous medium, *Proc. Camb. Phil. Soc.* **44,** 508–521 (1948).
10. H. Darcy, H., *Les Fontaines Publiques de la Ville de Dijon.* Victor Dalmond, Paris (1856).
11. S. V. Patankar and D. B. Spalding, A calculation procedure for heat, mass and momentum transfer in three-dimensional parabolic flows, *Int. J. Heat Mass Transfer* **15,** 1787–1806 (1972).
12. S. V. Patankar, A calculation procedure for two-dimensional elliptic situations, *Numer. Heat Transfer* **4,** 409–425 (1981).
13. F. W. Harlow and J. E. Welch, Numerical calculation of time-dependent viscous incompressible flow of fluid with free surface, *Phys. Fluids* **8,** 2182–2189 (1965).
14. R. J. A. Janssen, R. A. W. M. Henkes and C. J. Hoogendoorn, Transition to time-periodicity of a natural-convection flow in a 3D differentially heated cavity, *Int. J. Heat Mass Transfer* **36,** 2927–2940 (1993).
15. J. M. Mehta, Analysis of double-diffusive convection with temperature modulations at the boundaries, *Int. J. Heat Fluid Flow* **13,** 160–167 (1992).
16. A. Sarkar and O. M. Phillips, Effects of horizontal gradients on thermohaline instabilities in infinite porous media, *J. Fluid Mech.* **242,** 79–98 (1992).
17. A. Sarkar and O. M. Phillips, Effects of horizontal gradients on thermohaline instabilities in a thick porous layer, *Phys Fluids* **A4,** 1165–1175 (1992).
18. J. L. Lage, Effect of the convective inertia term on Bénard convection in a porous medium, *Numer. Heat Transfer* **A22,** 469–485 (1992).
19. W. V. Malkus, The heat transport and spectrum of thermal turbulence, *Proc. R. Soc. A* **225,** 196–212 (1954).
20. M. Combarnous and S. Bories, Modelisation de la convection naturelle au sein d'une couche poreuse horizontale a l'aide d'un coefficient de transfert solide–fluide, *Int. J. Heat Mass Transfer* **17,** 505–515 (1974).
21. F. H. Busse and D. D. Joseph, Bounds for heat transport in a porous layer, *J. Fluid Mech.* **54,** 521–543 (1972).
22. V. P. Gupta and D. D. Joseph, Bounds for heat transport in a porous layer, *J. Fluid Mech.* **57,** 491–514 (1973).
23. D. Nield and A. Bejan, *Convection in Porous Media.* Springer, New York (1992).